Electrical transport properties in Ge hyperdoped with Te

D. Caudevilla[1,*], S. Algaidy[1], F. Pérez-Zenteno[1], S. Duarte-Cano[1], R. García-Hernansanz[1], J. Olea[1], E. San Andrés[1], A. del Prado[1], R. Barrio[2], I. Torres[2], E. García-Hemme[1,*] and D. Pastor[1,*]

[1]Dpto. Estructura de la Materia, Física Térmica y Electrónica, Universidad Complutense de Madrid, Fac. de CC. Físicas. Plaza de Ciencias 1, E-28040 Madrid, Spain

[2]Unidad de Energía Solar Fotovoltaica, Dpto. de Energías Renovables, CIEMAT. Av. Complutense 40, E-28040 Madrid, Spain

E-mail: `danicaud@ucm.es`, `eric.garcia@ucm.es`, `dpastor@ucm.es`

July 2022

Abstract.

In this work we have successfully hyperdoped germanium with tellurium with a concentration peak of 10^{21} cm^{-3}. The resulting hyperdoped layers show good crystallinity and sub-bandgap absorption at room temperature which makes the material a good candidate for a new era of Complementary Metal-Oxide-Semiconductor (CMOS)-compatible short-wavelength-infrared (SWIR) photodetectors. We obtained absorption coefficients α higher than 4.1×10^3 at least up to 3 μm. In this study we report the temperature-dependency electrical properties of the hyperdoped layer measured in van der Pauw configuration. The electrical behaviour of this hyperdoped material can be explained with an electrical bilayer coupling/decoupling model and the values for the isolated hyperdoped layer are a resistivity of 4.25×10^{-3} Ω·cm with an electron-mobility around -100 cm^{2}V^{-1}s^{-1}.

Keywords: hyperdoping, tellurium, cryogenic ion implantation, bilayer model
Submitted to: *Semicond. Sci. Technol.*

1. Introduction

In the last years, short-wavelength-infrared (SWIR; 1-3 μm) detection has been attracting a great interest because its many applications, including biomedical imaging, surveillance, chemical sensing and long-haul-communications [1–3]. This market is dominated by group III-V and II-VI compounds such as InGaAs, InP, $Hg_{1-x}Cd_xTe$ [4,5]. However, these semiconductors are scarce, toxic and are not easily integrated with the read-out CMOS circuitry, which increases the size and cost of a final device. Moreover, most of these devices require cooling at liquid nitrogen temperature, increasing the dimensions and price of the device [6].

However, Si and Ge semiconductors are easily integrated with the standard CMOS technology. It has been demonstrated that the semiconductor can be hyperdoped introducing concentrations of deep-level donors such as Ti, Te, Se or Au with concentrations above the solid solubility limit. Some of these semiconductors exhibit sub-bandgap room- temperature photodetection. The reason for this response can be explained by the formation of an impurity band (IB). This band would allow the absorption of photons with energies not only above the bandgap energy, but also with lower energies. This absorption process promotes carriers from the valence band to the impurity band and from the impurity band to the conduction band [7–13]. Also, the signal-to-noise ratio of these hyperdoped devices is better than the conventional detectors and can be used at room temperature. Thus, these detectors could be easily incorporated into low-cost appliances, namely smart-phones. Several other materials based on hyperdoping and the IB concept have been studied since the 1960s and new materials are still being developed today for sub-banggap sensing, such as black diamond and hyperdoped-diamond [14, 15].

In this field, Si has been extensively studied, but there is an important lack of information about the Ge hyperdoped properties. In this work we focus on Ge because it already responds up to 1870 nm and the carrier mobilities are higher than in Si. There are different techniques to obtain hyperdoped materials [16], but in this work we focus on the combination of two out-of-the-equilibrium techniques: ion implantation followed by pulsed laser melting (PLM) [10,12]. With ion implantation we can introduce atoms at very high concentrations. In this case we have chosen tellurium because it is a deep-level donor in germanium, it already has high maximum solid solubility limit around $2{\times}10^{15}$ [17] and low diffusion coefficient (10^{-11} cm^{2}s^{-1} at 920 °C, [17]), which will allow us to incorporate more impurities to the lattice. After implantation, an ultra-fast recrystallization, using pulsed laser melting, is required to recover the crystallinity of the sample and activate the impurities while minimising the dopant diffusion.

The feasibility of the Ge hyperdoped with Te has already been proven [13]. In this work we study in detail the structural and optical properties of this material and focus on the electronic properties of the bilayer structure. We apply a bilayer model to the van der Pauw measurements and extract the electronic properties of the hyperdoped layer.

2. Experimental

2.1. Samples fabrication

A n-type germanium wafer (100) with a 300 μm thickness and 1 - 3 Ω·cm resistivity was implanted with ^{130}Te^{+} in a IBS refurbished VARIAN CF3000 ion implanter. The implantation energy set was 74 keV and the dose was 10^{15} cm^{-2}. The sample was tilted

7° to reduce channeling and the holder was refrigerated with liquid nitrogen (LN2) to avoid ion-implantation-related porosity [18–20]. This porosity effect has been attributed to the migration of the germanium vacancies forming clusters during the implantation process. It has been observed that this clustering process is very dependent on the temperature. We measured the temperature on the surface of the sample prior to the implantation and it was around 80 K.

After ion implantation, square-shaped samples were pulsed-laser melted (PLM) with a Nd:YAG laser working at its third harmonic wavelength (355 nm). The pulse duration was 4 ns and the energy 260 mJ, which corresponds to a fluence of 331 $\mathrm{mJ \cdot cm^{-2}}$ in a circular spot of 10 mm diameter. During this pulse, the top surface of the sample is melted beyond the amorphized region and afterwards it recrystallizes taking the substrate as seed, via solid-phase epitaxy. The speed of this recrystallization is so fast that the Te-impurities are trapped into the semiconductor lattice.

2.2. Structural characterization

Scanning Electron Microscopy (SEM) images were taken with a JEOL JSM 7600F working at 15 kV acceleration voltage to inspect the surface of the implanted samples.

We performed Time-of-Flight Secondary Ion Mass Spectroscopy (ToF-SIMS) to analyse the Te profile in depth. The experiments were done in negative polarity, obtained by a TOF-SIMS 4, manufactured by ION-TOF. $\mathrm{Bi^{3+}}$ was used as the primary ion at 25 keV pulsed beam tilted 45° for analysis and a Cs gun energy of 1 keV as sputtering source.

To check the crystal quality of the samples we used Raman spectroscopy with an excitation wavelength of 532 nm, which is absorbed approximately during the first 20 nm of the sample, so it gives us information about the implanted layer. We used a high resolution diffraction grating Echelle 75/64 and an objective of 20x/0.45. We focus on the Raman shift range from 163 to 196 $\mathrm{cm^{-1}}$, with a resolution of 0.22 $\mathrm{cm^{-1}}$.

2.3. Optical characterization

For the optical characterization we measure the transmittance $T(\lambda)$ and specular reflectance $R(\lambda)$ in normal incidence with a UV/Visible/NIR PerkinElmer Lambda 1050 spectrophotometer in the range 400 - 3000 nm. We calculate the total absorptance of the sample as $A(\lambda) = 1 - T(\lambda) - R(\lambda)$.

We can calculate the absorption coefficient of the implanted layer at wavelengths longer than the bandgap (1870 nm) if we follow some simplifying assumptions [11]:

- The substrate absorption coefficient is negligible and the thickness of the substrate is much higher than the wavelength, so we can neglect the interference effect on the calculations.
- The refractive index of the implanted layer is very similar to the one of the virgin Ge, so there is no refraction between the implanted layer and the substrate.

Then, the system can be modelled as a layer surrounded by air where the incoming light transmitted into the layer is reflected multiple times and each time that it is reflected there is some absorption. The total absorbance is the sum and can be expressed as a geometric series:

$$A(\lambda) = \sum_{n=0}^{\infty} I_0 ta(1-a)^n r^n = \frac{I_0 ta}{1 - r(1-a)}, \tag{1}$$

where I_0 is the incident intensity, $t \equiv t(\lambda)$ is the wavelength-dependent transmission coefficient between air and Si, $r \equiv r(\lambda)$ is the reflection coefficient for each wavelength between Si and air, and $a(\lambda)$ is the absorption term resulting from each time light travels through the implanted layer. This term is defined as $a(\lambda) = \exp(-\alpha d)$, where $\alpha \equiv \alpha(\lambda)$ is the absorption coefficient and d is the effective thickness of the absorbing layer. We can apply the same model to extract the absolute transmitted and reflected light after multiple reflections. These expressions also follow a geometric series and their sum is equal to the incident light.

2.4. Electrical characterization

Some samples were cut in square shape and 200 nm Ni contacts were deposited by e-beam evaporation on the corners, in van der Pauw configuration. The contacts were connected through 4 SMU probes to a Keithley SCS 4200 model and the samples were kept inside a Janis cryostat which allows us to measure from 300 K to 15 K. We measured the sheet conductance (G_S) in the four possible configurations feeding with 1 mA. The current was injected in both directions, thus we measured eight configurations in total. We also measured the Hall effect injecting the current in opposite contacts and applying a 0.9 T magnetic field. This magnetic field was also applied in both perpendicular directions to the sample, resulting in sixteen configurations for the Hall effect. The electromagnet was powered with a bipolar Kepco BOP 50–20MG power supply.

To analyse the behaviour of the hyperdoped samples we apply the bilayer model proposed in [21], since the hyperdoped layer is electrically coupled to the substrate depending on the temperature. This model describes the electrical properties of a two-layers system:

$$G_S = \frac{\ln 2}{\pi} \frac{I}{\Delta V} = \frac{(G_{S1} + G_{S2}F)^2}{G_{S1} + G_{S2}F^2} \tag{2}$$

$$\mu = -\frac{G_S \Delta V_{HALL}}{IB} = \frac{\mu_1 G_{S1} + \mu_2 G_{S2} F^2}{G_{S1} + G_{S2}F^2}, \tag{3}$$

where G_S is the measured sheet conductance of the bilayer system, and it is the result of the combination of the sheet conductance of each layer ($G_{S1,2}$). In a similar way, the mobility (μ) of the system is given by the average mobilities weighted by the conductance of each layer ($\mu_{1,2}$). The contribution of the substrate (G_{S2} and μ_2) to the measurement depends on the coupling factor F, which varies form 0 to 1. In the regions where the F parameter is known we can extract the properties of the implanted layer.

3. Results and discussion

3.1. Structural results

Ion implantation at LN2 temperature has been realised to avoid surface porosity [18]. In figure 1 we show the surface morphology obtained by SEM of the implanted samples at a) LN2 and b) room temperature. The sample implanted at room temperature is fully porous and the sample implanted at LN2 temperature shows a similar surface than an unimplanted sample, corroborating that implanting at LN2 temperatures avoids the formation of porous structures.

In figure 2 we show the measured Te concentration depth profile for an as-implanted sample and a sample after the laser melting obtained by ToF-SIMS. It is also represented the Monte-Carlo SRIM simulation of a 74 keV implantation at RT. We can observe that the Te profile of the as-implanted sample does not follow the SRIM simulation. When implanting at LN2 temperatures, the profile is shifted closer to the surface. During the implantations we also implanted control samples with lithography structures and we did not observe significant differences in topography between the implanted and unimplanted regions, which rules out the possibility of a relevant sputtering during the implantation. The explanation for this difference between the measured profile shifted to the surface and the SRIM simulation is not clear but has also been observed when implanting different ions at low temperatures in other materials [22]. Even with this discrepancy between simulation and experiments, these results demonstrate that we have overcame the solid solubility limit of Te in Ge by more than five orders of magnitude in the first 23 nm.

After the pulsed laser melting process, the Te impurities have been redistributed around the first 10 nm, where we have a maximum concentration of 1.1×10^{21} cm^{-3}. The impurity concentration to surpass the insulator to metal transition and form an impurity band is nominally 5.9×10^{19} cm^{-3}, but depends on the host semiconductor and the impurity [8]. We overcome the insulator to metal transition in the first 35 nm and the solid solubility limit in the fully implanted region. For the calculations during this work we will take 35 nm as the reference effective thickness of the hyperdoped layer.

In figure 3 we show the Raman spectra for the germanium reference sample, the as-implanted sample, and the pulsed laser melted sample. During the implantation, the sample surfaces become amorphous and this pointed out by the a-Si band around 250-300 cm^{-1} of the implanted spectrum. We do not observe any crystalline signal in the as-implanted samples, meaning that all the light is absorbed in the implanted region. However, after the PLM process, the crystallinity of the sample is fully recovered, as the crystalline Ge-Ge peak at 300 cm^{-1} indicates. This peak is almost identical in shape as the peak from a Ge reference sample. The observed downshift of less than 1 cm^{-1} would be related to lattice strain due to the Te incorporation in the Ge lattice.

3.2. Optical results

3.2.1. Transmittance. After producing a high crystallinity implanted layer with Te concentration well above its solid solubility limit, we measure the transmittance and reflectance to determine the optical activation of that impurities. First, we measure the transmittance of the samples (figure 4a). Light up to 1870 nm (band-gap of Ge: 0.66 eV) is either reflected in the substrate or absorbed in the substrate. For longer wavelengths, the substrate is not absorbing, so the transmittance difference between the reference sample and the implanted samples is because of multiple reflections or the absorption of the implanted layer.

3.2.2. Reflectance. In figure 4b we have represented the reflectance measurements. In the reference sample we can clearly observe that the reflectance comes from the reflectance of the top surface for wavelengths below 1870 nm; and above, the reflected light comes from the top surface reflectance but also from the back surface, since the germanium is transparent at those wavelengths. The as-implanted sample differs from the reference at sub-bandgap wavelengths due to the amorphization of the implanted layer. At wavelengths above Ge bandgap, the reflectance is slightly reduced most probably because the induced defects are absorbing part of the light [23]. However, the PLM sample recovers a shape of the curve very similar to the Ge substrate, which was expected because we recovered the crystallinity. However, after the PLM, the sample recovers the crystallinity, since it can be observed to have a similar behaviour than the Ge substrate. Furthermore, in the PLM sample, the reflectance is lower for wavelengths above the bandgap, and this can be explained with the absorption of the hyperdoped layer. The reflectance of the PLM is also lower for wavelengths below 750 nm, most probably because the refractive index is changed at those wavelengths.

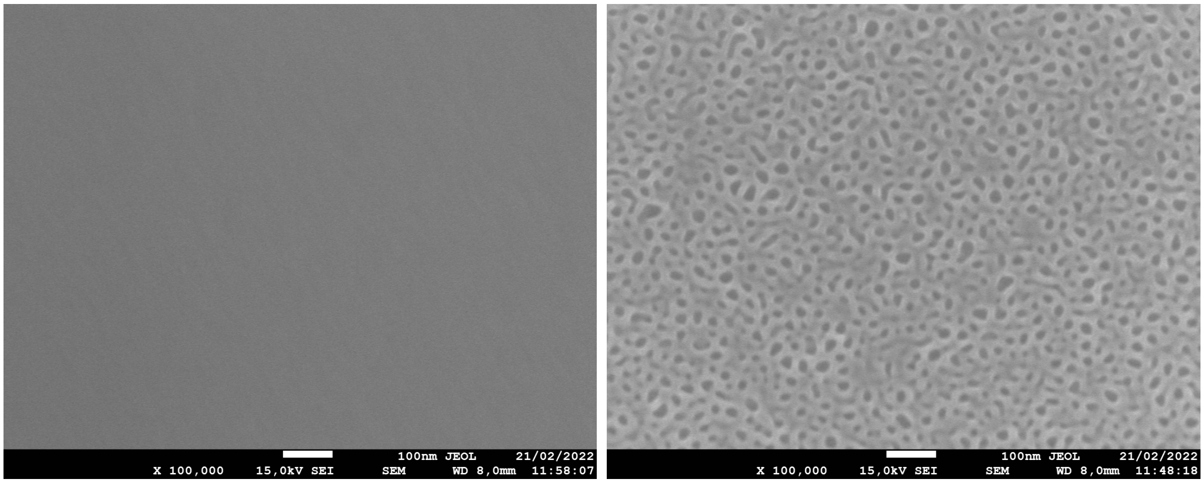

Figure 1: SEM images of the surface of Te-implanted Ge with a dose of 10^{15} cm^{-2} at different temperatures: a) liquid-nitrogen temperature and b) room temperature.

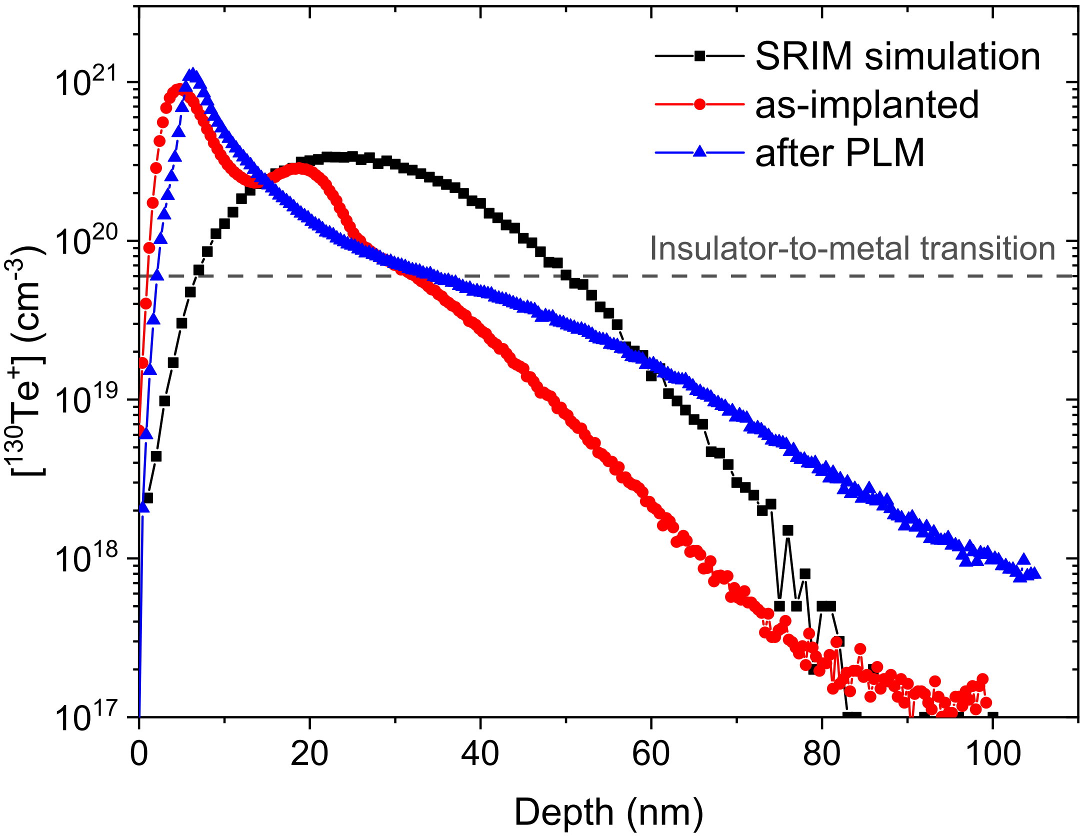

Figure 2: ToF-SIMS measurements of as- implanted and PLM samples together with the SRIM simulation at RT. It is also highlighted the insulator to metal transition [8].

3.2.3. Absorptance. Subtracting the transmittance and the reflectance to the 100% we can obtain the light which is absorbed in our samples (figure 5). If we focus on the wavelengths longer than 1870 nm (which corresponds to 0.66 eV, the energy of the bandgap), we corroborate that the absorptance of the reference Ge sample is negligible. The physical reason behind this is that the energy of the photons is not enough to overcome the bandgap energy ($E<E_{gap}$) and they are not absorbed. For the as-implanted sample, around 2% of the light is absorbed in the implanted region, most probably because of defects and the amorphous character of the layer. The PLM-recrystallized sample has even higher absorptance than the as-implanted sample. Also, as it has been shown by Raman spectroscopy, it exhibits better crystal quality. Thus, we associate this sub-bandgap absorption to extrinsic defects introduced by the ion implantation followed by the pulsed laser melting process. The total absorption of this sample is around 4%, and applying the equations given in section 2.3 it corresponds to a factor αd of 4.1×10^{-2}, which is in agreement with the values previously reported for similar doses [13]. If we consider that the layer depth where we overcome the insulator to metal transition (35 nm) is the thickness of the absorbing layer above 1870 nm we can set an upper limit for the absorption coefficient of $1.2{\times}10^4$ cm^{-1}, and taking 100

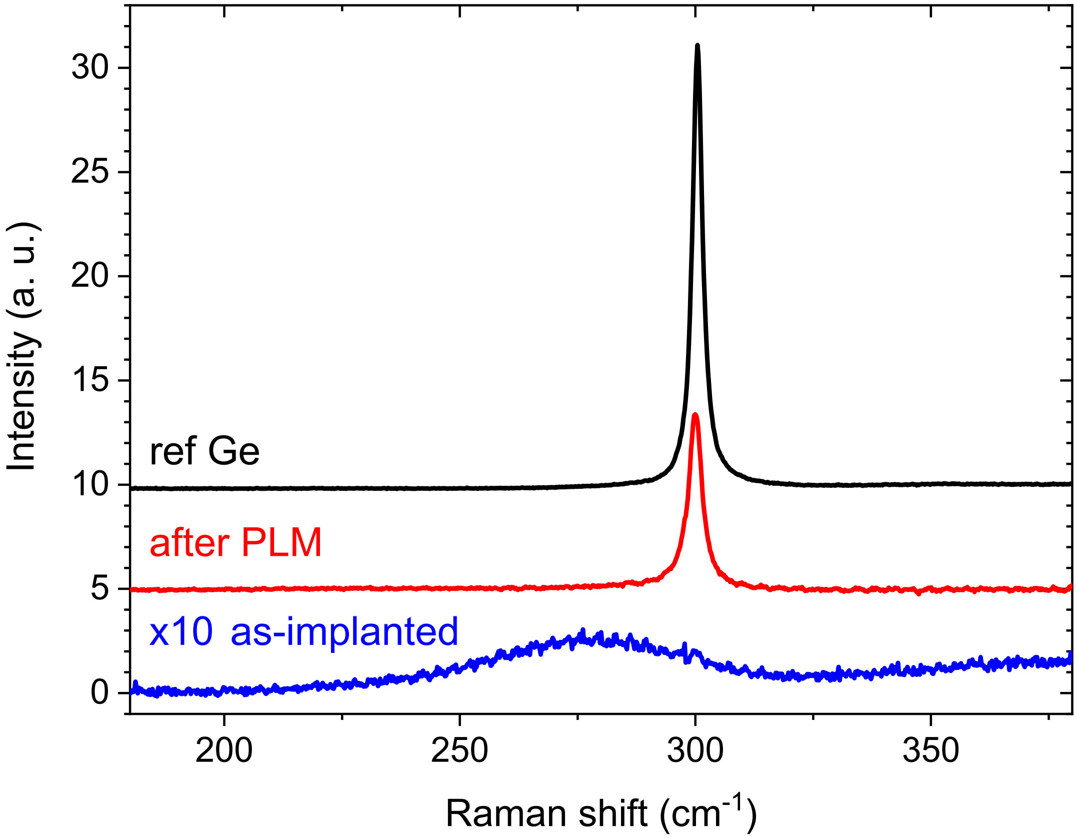

Figure 3: Raman spectra of a virgin Ge sample, a Te as-implanted amorphized sample and a Te-implanted sample recrystallized by PLM (for the sake of clarity, the spectra are shifted vertically).

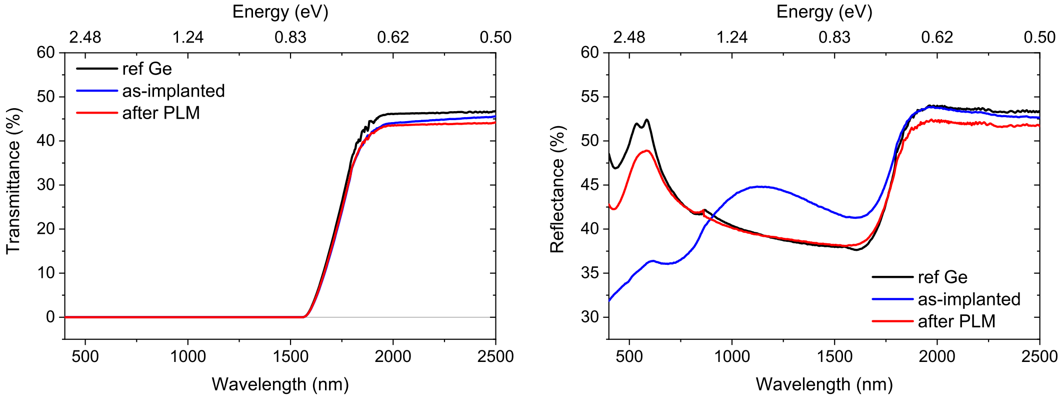

Figure 4: Optical measurements: Transmittance (left) and reflectance (right) of a reference Ge sample, an as-implanted sample and a recrystallized PLM sample.

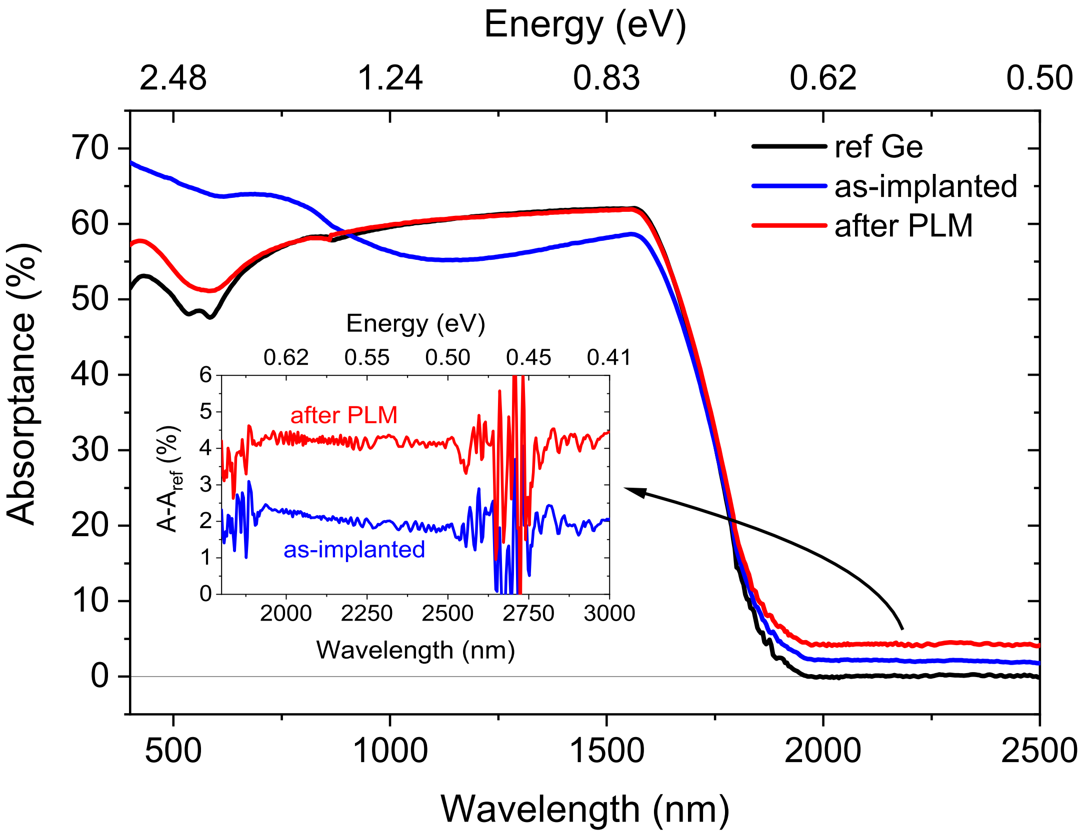

Figure 5: Absorptance of a reference Ge-sample, a Te-implanted sample and a recrystallized Ge:Te sample. In the inset it is plotted the absorption difference in % between the implanted samples with respect to the reference Ge sample for wavelengths between 2000 and 3000 nm

.

nm as the thickness of the absorbing layer we set the lower limit to 4.1×10^3 cm^{-1}. The most probable scenario is that the implanted layer is changing the absorption coefficient according to the tellurium profile and the total absorptance comes from integrating the whole profile. In any case those limits show that the absorption coefficient is more than 5 orders of magnitude higher than for virgin Ge, in agreement with previous results [13]. These values are in the same order of magnitude as the highest absorption coefficients obtained from hyperdoped silicon [11, 24].

3.3. Electrical results

The electrical properties of the hyperdoped layer on n-type substrates present a temperature-dependence decoupling effect, as shown in figure 6. In this graph, it can be observed that the sheet conductance (G_S) tendency of the implanted sample is similar to the sheet conductance of a measured substrate (G_{S2}) for temperatures ranging from 300 K down to 200 K, so in this region we conclude that both layers are totally coupled

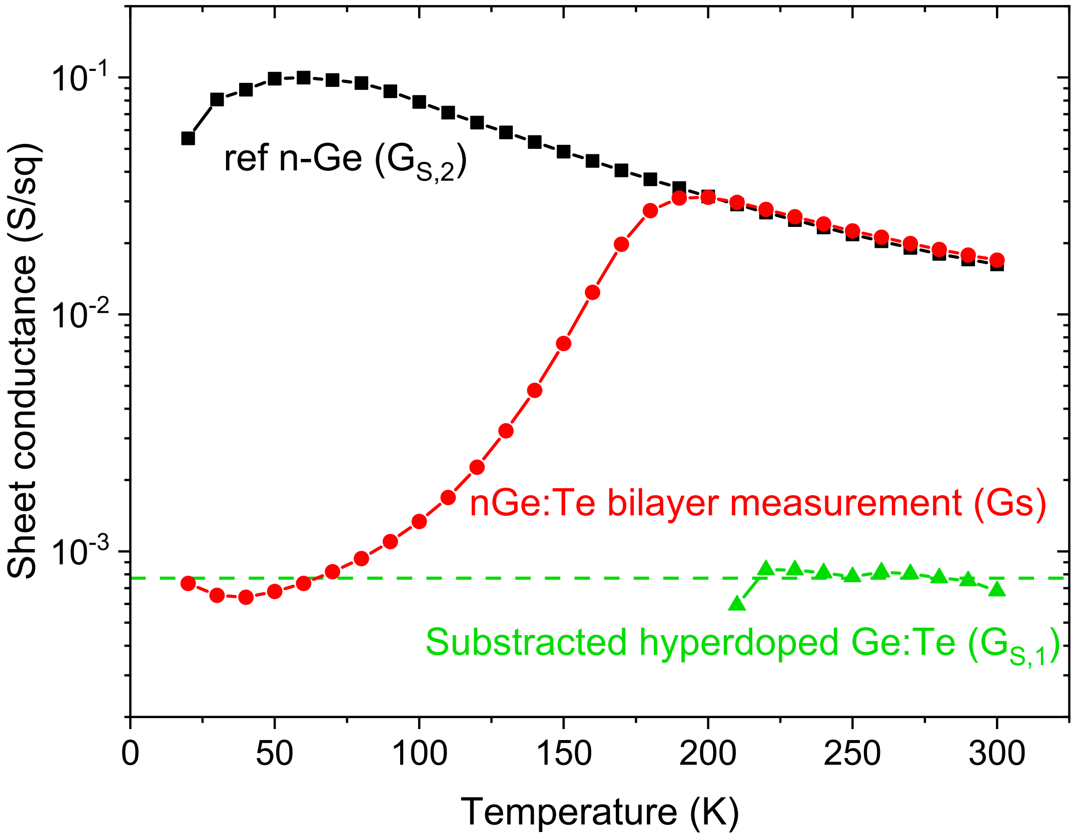

Figure 6: Sheet conductance (G_S) of a reference n-Ge substrate (■) and a Te-implanted sample and recrystallized by PLM (●). It is also represented the sheet resistance extracted values of the hyperdoped layer with a guide to the ere with the mean value in the region from 200 to 300 K.

($F = 1$). As the temperature decreases, the hyperdoped layer starts to be electrically decoupled from the substrate ($F < 1$), unveiling the properties of the hyperdoped layer as if it would be isolated. In figure 7, the differences between the reference Ge sample and the hyperdoped sample can be observed. As expected, the mobility of the reference sample increases as the temperature decreases as a result of a lower interaction with the phonons of the lattice. In contrast, for the hyperdoped sample, the mobility decreases as the temperature decreases, which falls down reaching values around -100 cm^{2}V^{-1}s^{-1} for temperatures in the 20-100 K region. The measured mobility is electron-dominated for the whole range of temperatures (20-300 K). These results are in good agreement with previously reported results of similar hyperdoped structures, such as Si:Ti [21] and Si with other transition metals (Cr, V) [25].

If we apply the model described in 2.4 with $F = 1$ in the region where the layers are totally coupled, we can extract the values of the sheet conductance of the hyperdoped layer, which is shown in figure 6, just by subtracting the sheet conductance of the substrate to the measured value. We can observe that these values are constant among

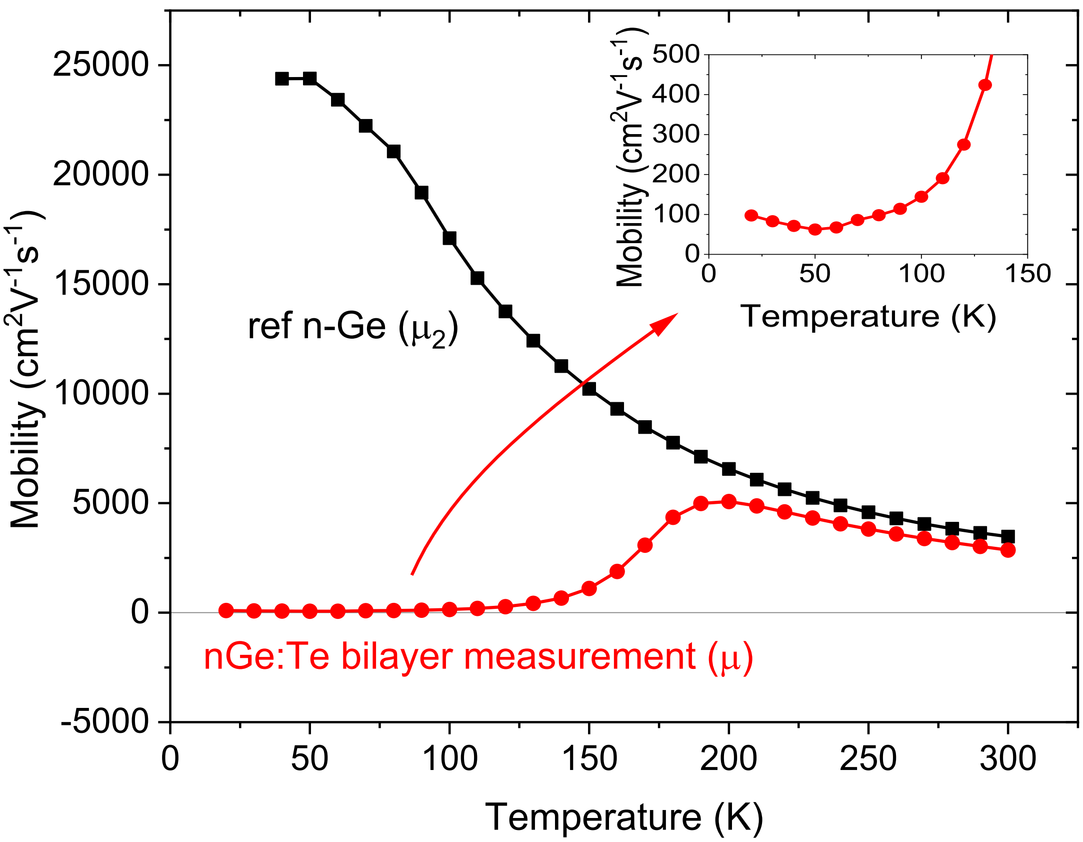

Figure 7: Measured hall mobility as a function of the temperature in van der Pauw configuration of a reference sample and an implanted and PLM sample. The inset is a zoom in the 0-150 K temperatures region for the values of the hyperdoped sample.

that region, as it is expected from a hyperdoped metallic layer, and it is also plotted a dashed line of the mean value as a guide to the eye, since this value is in the same order of the sheet conductance values of the bilayer system when the implanted layer is isolated from the substrate. These values correspond to 235 S·cm^{-1} if we consider that the thickness of the layer is the depth where we overcome the insulator to metal transition. For mobility and sheet concentration measurements we cannot apply the model because the differences between the sheet conductance multiplied by the mobility of both measurements are very similar; then the error is high: for example, a difference of just a 5% in the mobility or concentration of the substrate parameters means a variation on the layer mobility values from -10000 to 1800 cm^{2}V^{-1}s^{-1}, which is not consistent and makes no physical sense. To better analyse the electrical properties of this system it is convenient to implant higher doses, and then the implanted layer will increase the contribution to the measured values.

The measured values at low temperature correspond to electrical measurements of the isolated hyperdoped layer. This layer presents a conductivity of 235 S·cm^{-1}, a mobility of -100 cm^{2}V^{-1}s^{-1} and an effective electron carrier concentration of around

1.5×10^{19} cm^{-3}. This carrier concentration is slightly lower than the theoretical insulator to metal transition concentration for the impurity band formation. Since we observe at low temperature the metallic behaviour associated to the impurity band formation, this threshold could be lower for this specific system formed by the Ge and the Te, or the effective thickness considered for the hyperdoped semiconductor is slightly lower. In any case the carrier concentration value is several orders above the solid solubility limit and in the order of the theoretical insulator to metal transition limit.

4. Conclusion

In this work we have successfully implanted Ge with Te with a peak concentration of 10^{21} cm^{-3} recovering the crystallinity of the samples after a laser annealing process. We obtain a crystalline hyperdoped layer which overcomes the insulator to metal transition the first 35 nm showing sub-bandgap absorption at room temperature and an absorption coefficient around 1.2×10^{4} in agreement with previous reports. We analysed the electrical properties of the implanted samples and observe a temperature-dependency coupling effect very similar to other hyperdoped materials which are also suitable for infrared sensing.

Using an electrical bilayer model, we can explain the electrical measured behaviour assuming an electrical decoupling of the hyperdoped and Ge substrate layers. Since the hyperdoped layer is electrically isolated at low temperatures we can measure the electrical transport measurements of the hyperdoped semiconductor.

Acknowledgments

Authors wish to acknowledge assistance from CAI de Ciencias Físicas (Unidad de Implantación Iónica) and CAI de Ciencias Químicas (Espectroscopía Raman y Correlación) from the Universidad Complutense de Madrid with the Ion Implantations and Raman measurements, respectively. We also acknowledge Servicio de Nanotecnología y Análisis de Superficies del CACTI de la Universidad de Vigo for ToF-SIMS measurements and ICTS-CNM from Madrid for the SEM images. This work was partially supported by the projects MADRID-PV2 (P2018/EMT-4308) funded by the Comunidad Autónoma de Madrid with the support from FEDER Funds and projects SCCell (PID2020-116508RB-I00), HyperPHIR (PID2020-117498RB-I00) and SCALED (PID2019-109215RB-C42), funded by the Spanish Ministry of Science and Innovation. D. Caudevilla would also acknowledge the grant PRE2018-083798, financed by MICINN and European Social Fund. F. Pérez-Zenteno would also like to acknowledge grant 786327 form Mexican grants program CONACyT.

Supplementary material

Equations used for transmittance and reflectance considering multiple reflections between the hyperdoped layer and air:

$$\begin{aligned} R &= I_0 r + I_0 t^2 r(1-a)^2 + I_0 t^2 r^3 (1-a)^4 + I_0 t^2 r^5 (1-a)^6 + ... \\ &= I_0 r + I_0 r t^2 (1-a)^2 \sum_{n=0}^{\infty} [r(1-a)]^{2n} = I_0 r \left[1 + \frac{t^2(1-a)^2}{1-r^2(1-a)^2} \right] \end{aligned} \tag{4}$$

$$\begin{aligned} T &= I_0 t^2 (1-a) + I_0 t^2 r^2 (1-a)^3 + I_0 t^4 r^2 (1-a)^5 + ... \\ &= I_0 t^2 (1-a) \sum_{n=0}^{\infty} [r(1-a)]^{2n} = \frac{I_0 t^2 (1-a)}{1-r^2(1-a)^2} \end{aligned} \tag{5}$$

References

[1] Marc P. Hansen and Douglas S. Malchow. Overview of SWIR detectors, cameras, and applications. In *Thermosense XXX*, volume 6939, pages 94–104. SPIE, March 2008.

[2] Richard Soref. Enabling 2 μm communications. *Nature Photonics*, 9(6):358–359, June 2015. Number: 6 Publisher: Nature Publishing Group.

[3] Yonder Berencén, Slawomir Prucnal, Wolfhard Möller, René Hübner, Lars Rebohle, Roman Böttger, Markus Glaser, Tommy Schönherr, Ye Yuan, Mao Wang, Yordan M. Georgiev, Artur Erbe, Alois Lugstein, Manfred Helm, Shengqiang Zhou, and Wolfgang Skorupa. CMOS-Compatible Controlled Hyperdoping of Silicon Nanowires. *Advanced Materials Interfaces*, 5(11):1800101, 2018. _eprint: https://onlinelibrary.wiley.com/doi/pdf/10.1002/admi.201800101.

[4] S. Manda, R. Matsumoto, S. Saito, S. Maruyama, H. Minari, T. Hirano, T. Takachi, N. Fujii, Y. Yamamoto, Y. Zaizen, T. Hirano, and H. Iwamoto. High-definition Visible-SWIR InGaAs Image Sensor using Cu-Cu Bonding of III-V to Silicon Wafer. In *2019 IEEE International Electron Devices Meeting (IEDM)*, pages 16.7.1–16.7.4, December 2019. ISSN: 2156-017X.

[5] R. K. Bhan and V. Dhar. Recent infrared detector technologies, applications, trends and development of HgCdTe based cooled infrared focal plane arrays and their characterization. *Opto-Electronics Review*, 27(2):174–193, June 2019.

[6] Nikolai G. Kalugin, Lei Jing, Wenzhong Bao, Lee Wickey, Christopher Del Barga, Mekan Ovezmyradov, Eric A. Shaner, and Chun Ning Lau. Graphene-based quantum Hall effect infrared photodetector operating at liquid Nitrogen temperatures. *Applied Physics Letters*, 99(1):013504, July 2011. Publisher: American Institute of Physics.

[7] Antonio Luque and Antonio Martı. Increasing the Efficiency of Ideal Solar Cells by Photon Induced Transitions at Intermediate Levels. *PHYSICAL REVIEW LETTERS*, 78(26):4, 1997.

[8] Antonio Luque, Antonio Martí, Elisa Antolín, and César Tablero. Intermediate bands versus levels in non-radiative recombination. *Physica B: Condensed Matter*, 382(1):320–327, June 2006.

[9] Yonder Berencén, Slawomir Prucnal, Fang Liu, Ilona Skorupa, René Hübner, Lars Rebohle, Shengqiang Zhou, Harald Schneider, Manfred Helm, and Wolfgang Skorupa. Room-temperature short-wavelength infrared Si photodetector. *Scientific Reports*, 7(1):43688, March 2017. Number: 1 Publisher: Nature Publishing Group.

[10] Eric García-Hemme, Daniel Caudevilla, Sari Algaidy, Francisco Pérez-Zenteno, Rodrigo García-Hernansanz, Javier Olea, David Pastor, Álvaro del Prado, Enrique San Andrés, Ignacio Mártil, and Germán González-Díaz. On the Optoelectronic Mechanisms Ruling Ti-hyperdoped Si Photodiodes. *Advanced Electronic Materials*, 8(2):2100788, 2022. _eprint: https://onlinelibrary.wiley.com/doi/pdf/10.1002/aelm.202100788.

[11] Jonathan P. Mailoa, Austin J. Akey, Christie B. Simmons, David Hutchinson, Jay Mathews, Joseph T. Sullivan, Daniel Recht, Mark T. Winkler, James S. Williams, Jeffrey M. Warrender, Peter D. Persans, Michael J. Aziz, and Tonio Buonassisi. Room-temperature sub-band gap optoelectronic response of hyperdoped silicon. *Nature Communications*, 5(1):3011, May 2014.

[12] Hemi H. Gandhi, David Pastor, Tuan T. Tran, S. Kalchmair, L.A. Smilie, Jonathan P. Mailoa, Ruggero Milazzo, Enrico Napolitani, Marco Loncar, James S. Williams, Michael J. Aziz, and Eric Mazur. Gold-Hyperdoped Germanium with Room-Temperature Sub-Band-Gap Optoelectronic Response. *Physical Review Applied*, 14(6):064051, December 2020.

[13] Hemi H. Gandhi, David Pastor, Tuan T. Tran, Stefan Kalchmair, Lachlan A. Smillie, Jonathan P. Mailoa, Ruggero Milazzo, Enrico Napolitani, Marko Loncar, James S. Williams, Michael J. Aziz, and Eric Mazur. Chalcogen-hyperdoped germanium for short-wavelength infrared photodetection. *AIP Advances*, 10(7):075028, July 2020. Publisher: American Institute of Physics.

[14] Paolo Calvani, Alessandro Bellucci, Marco Girolami, Stefano Orlando, Veronica Valentini, Riccardo Polini, and Daniele M. Trucchi. Black diamond for solar energy conversion. *Carbon*, 105:401–407, August 2016.

[15] Xiao Dong, Rong Qiao, Tianxing Wang, Yipeng An, and Yongyong Wang. Engineering a bandgap-regulable intermediate-band material based on diamond. *Carbon*, 191:106–111, May 2022.

[16] Sheng-Xiang Ma, Xiao-Long Liu, Hai-Bin Sun, Yang Zhao, Yue Hu, Xi-Jing Ning, Li Zhao, and Jun Zhuang. Enhanced responsivity of co-hyperdoped silicon photodetectors fabricated by femtosecond laser irradiation in a mixed SF_6/NF_3 atmosphere. *JOSA B*, 37(3):730–735, March 2020. Publisher: Optica Publishing Group.

[17] W. W. Tyler. Deep level impurities in germanium. *Journal of Physics and Chemistry of Solids*, 8:59–65, January 1959.

[18] O. W. Holland, B. R. Appleton, and J. Narayan. Ion implantation damage and annealing in germanium. *Journal of Applied Physics*, 54(5):2295–2301, May 1983.

[19] L. Romano, G. Impellizzeri, M. V. Tomasello, F. Giannazzo, C. Spinella, and M. G. Grimaldi. Nanostructuring in Ge by self-ion implantation. *Journal of Applied Physics*, 107(8):084314, April 2010. Publisher: American Institute of Physics.

[20] Giuliana Impellizzeri, Lucia Romano, Lorenzo Bosco, Corrado Spinella, and Maria Grazia Grimaldi. Nanoporosity Induced by Ion Implantation in Germanium Thin Films Grown by Molecular Beam Epitaxy. *Applied Physics Express*, 5(3):035201, March 2012. Publisher: IOP Publishing.

[21] J. Olea, G. González-Díaz, D. Pastor, I. Mártil, A. Martí, E. Antolín, and A. Luque. Two-layer Hall effect model for intermediate band Ti-implanted silicon. *Journal of Applied Physics*, 109(6):063718, March 2011.

[22] Masataka Kase, Yoshio Kikuchi, Mami Kimura, Haruhisa Mori, and Reuel B. Liebert. Defects produced in Si p^+n diodes by B^+ implantation at liquid nitrogen temperature or -60 °C. *Journal of Applied Physics*, 75(7):3358–3364, April 1994.

[23] Stephen K. O'Leary, Stefan Zukotynski, and John M. Perz. Disorder and optical absorption in amorphous silicon and amorphous germanium. *Journal of Non-Crystalline Solids*, 210(2):249–253, March 1997.

[24] J. Olea, A. del Prado, D. Pastor, I. Mártil, and G. González-Díaz. Sub-bandgap absorption in Ti implanted Si over the Mott limit. *Journal of Applied Physics*, 109(11):113541, June 2011. Publisher: American Institute of Physics.

[25] Eric García-Hemme, Rodrigo García-Hernansanz, Javier Olea, David Pastor, Alvaro del Prado, Ignacio Mártil, and Germán González-Díaz. Meyer Neldel rule application to silicon supersaturated with transition metals. *Journal of Physics D: Applied Physics*, 48(7):075102, February 2015.